JOURNAL OF SPACECRAFT AND ROCKETS
Vol. 48, No. 2, March–April 2011

Analysis of Transient Flow in Supersonic Micronozzles

William F. Louisos* and Darren L. Hitt†
University of Vermont, Burlington, Vermont 05405

DOI: 10.2514/1.51027

A numerical investigation of transient supersonic flow through a two-dimensional linear micronozzle has been performed. The baseline model for the study is derived from the NASA Goddard Space Flight Center microelectromechanical-systems-based hydrogen peroxide prototype microthruster. A hyperbolic-tangent actuation profile is used to simulate the opening and closing of a microvalve with a maximum inlet stagnation pressure of 250 kPa, which generates a maximum throat Reynolds number of $Re \sim 800$. The complete duty cycle occurs over 1.7 ms. Numerical simulations have been conducted for expander half-angles of 10–50°, and both slip and no-slip wall boundary conditions have been examined. The propulsion scheme employs 85%-pure hydrogen peroxide as the monopropellant fuel. Simulation results have been analyzed, and thrust production as a function of time has been quantified, along with the total impulse delivered. Micronozzle impulse efficiency has also been determined based on a theoretical maximum impulse achieved by a quasi-1-D inviscid flow responding instantaneously to the actuation profile. It is found that both the flow and thrust exhibit a response lag to the time-varying inlet pressure profile. Simulations indicate that a maximum efficiency and impulse occur for an expander half-angle of 30° for the no-slip wall boundaries, and the slip simulations demonstrate a maximum plateau in the range of 20–30°; these angles are significantly larger than with traditional conical nozzle designs.

Nomenclature

A	=	area, m^2
E	=	total energy, J
$\mathbf{F}$	=	thrust, N
g	=	gravity, 9.8 m/s^2
h	=	enthalpy, J
I	=	impulse, $(N \cdot s)/m$
L	=	characteristic length scale, m
k	=	thermal conductivity, $W/(m \cdot K)$
$\dot{m}$	=	mass flow rate, kg/s
n	=	unit normal vector
p	=	pressure, Pa
R	=	gas constant, $J/(kg \cdot K)$
Re	=	Reynolds number
T	=	temperature, K
t	=	time, s
$\mathbf{V}$	=	velocity vector, m/s
γ	=	ratio of specific heats
η	=	nozzle impulse efficiency, %
θ	=	expander half-angle, °
μ	=	dynamic viscosity, $kg/(m^2 \cdot s)$
ρ	=	density, kg/m^3
τ	=	viscous stress tensor, Pa

Subscripts

exit	=	nozzle exit conditions
f	=	final
i	=	initial
max	=	maximum
0	=	stagnation condition
∞	=	ambient condition

Superscript

*	=	throat condition

Presented as Paper 2006-2874 at the 36th AIAA Fluid Dynamics Conference and Exhibit, San Francisco, CA, 5–8 June 2006; received 8 June 2010; revision received 30 November 2010; accepted for publication 13 December 2010.

*Lecturer, Mechanical Engineering Program, School of Engineering, 33 Colchester Avenue; William.Louisos@uvm.edu. Member AIAA.

†Associate Professor, Mechanical Engineering Program, School of Engineering, 33 Colchester Avenue; Darren.Hitt@uvm.edu. Member AIAA.

I. Introduction

MICROELECTROMECHANICAL systems (MEMS) techniques offer great potential in satisfying future mission requirements for the next generation of small-scale spacecraft being designed by NASA and U.S. Department of Defense agencies. These miniaturized spacecraft, more commonly referred to as nanosatellites (nanosats) or picosatellites (picosats), feature masses in the range of 1–20 kg. Because of the substantially reduced size, nanosats have unique propulsion requirements, including extremely low thrust levels and/or extremely low minimum impulse requirements for orbital maneuvers and attitude control [1,2]. A comprehensive discussion of small-satellite technologies and technical challenges can be found in the recent monograph by Helvajian and Janson [3]. Surveys of micropropulsion systems and microthruster options can also be found in reviews by Mueller [4] and Reichbach et al. [5].

A key component in microthruster design based upon either solid or chemical propellants is the converging–diverging supersonic nozzle. Upstream of the nozzle inlet, the propellant undergoes combustion and/or chemical decomposition, which releases thermal and pressure energy. The role of the supersonic nozzle is to convert this available energy into kinetic energy and thrust. Recent studies have shown that supersonic micronozzle flows can differ greatly from their macroscale counterparts, in that they can be greatly impacted by viscous forces due to the very low Reynolds numbers, rarefaction effects due to relatively large Knudsen numbers, and heat transfer due to the large ratio of substrate surface area to fluid volume.

In the study of micronozzle flow, there exists a key performance tradeoff between viscous effects and expander geometry. For various microscale nozzles reported in the literature, the Reynolds numbers are relatively low. Typical values are below 1000 during steady-state operation and often less than 100 during transient operation. Even smaller Reynolds number are prevalent during startup and shutdown of the thruster when reduced inlet pressures are unavoidable. Small pressure gradients result in low mass flow rates, reduced flow velocities, and thus very small Reynolds numbers: often on the order of $Re \sim 10$. As such, the magnitude of viscous losses can be

significant. From this, the expander section experiences large subsonic boundary-layer growth that can extend a sufficient distance away from the wall so as to reduce the bulk flow and lower nozzle efficiency. To compensate for this, some designs have proposed increased expander angles; however, this introduces potential performance reductions, due to nonaxial exit flow. A velocity component in the lateral direction greatly reduces micronozzle thrust output and efficiency.

Positioning of the spacecraft is achieved by applying discrete impulse bits, and so the impulse delivered by the micronozzle is a key parameter of interest. The use of quasi-1-D theory can lead to errors in performance calculations on the microscale, due to the tradeoff between viscous forces and geometric losses. It is possible that impulse shortages can result from a viscous delay in flow response to transient inlet conditions or if expander angles are made too large when attempting to compensate for viscous effects.

Viscous effects in supersonic micronozzle flow were first investigated by Bayt and Breuer [6,7], who demonstrated that the subsonic layer can occupy a significant fraction of the expander flowfield, reducing flow and resulting in thrust loss. Alexeenko et al. [8–13] and Ketsdever et al. [14] have performed extensive direct simulation Monte Carlo (DSMC) simulations of micronozzle flow for cold-gas thrusters with 2-D axisymmetric and, to a lesser degree, 3-D geometries. The effects of geometry and reduced ambient backpressure on micronozzle flows have been explored by Choudhuri et al. [15] for conical 15 and 20° bell- and trumpet-shaped diverging nozzle sections. Experimental studies were performed and color schlieren imaging was used to visualize the flow regime inside the nozzle. It was shown that the flow regime in a micronozzle is viscous-dominated and that viscous effects play a key role in thruster performance.

All of the published work has primarily dealt with steady-state cold-gas flows, and limited nozzle geometries have been considered. As the operation of a microthruster firing is an inherently transient operation resulting from its intended role of spacecraft attitude adjustment, this is an important consideration, and the flow and thrust response on the microscale needs to be delineated. The premise is that viscous forces introduce an additional time scale, separate from the external time scale of the thruster firing (e.g., valve opening and closing). As such, there is a potential for a lag in thrust production and a discrepancy between the ideal and actual thrust profiles and impulse delivered during a firing. The only studies to consider transient flows include our preliminary work from 2006 [16], the conference paper by Kujawa and Hitt [17], and the paper by Morinigo and Quesada [18]. Morinigo and Quesada use a continuum-based model to investigate viscous heating of the nozzle substrate during a single rocket firing with hot and cold N_2 gas as the working fluid. The primary limitation of this work is that it examines only a single-nozzle geometry. In this regard, our current study nicely complements and extends the existing micronozzle literature through examination of monopropellant-based micronozzles with varying expander geometries and both slip and no-slip wall boundary conditions.

In this paper, we report the key findings from transient simulations of supersonic micronozzle flows for a complete duty cycle (single firing) with realistic MEMS-valve actuation profiles while varying expander half-angles from 10–50° and considering decomposed hydrogen peroxide (H_2O_2) as the monopropellant. This study thus represents an important and necessary contribution to the existing micronozzle literature.

II. Computational Model

In designing a MEMS-scale supersonic nozzle, microfabrication considerations necessitate nozzle geometries in the form of rectangular ducts and so are *not axisymmetric* like their macroscale counterparts. Macroscale thrusters often feature outlet nozzles with contoured walls (e.g., bell or trumpet shapes) for the purposes of straightening the outlet flow and producing a uniaxial thrust normal to the exit plane. Microfabrication of such symmetric wall contours is generally difficult especially in terms of reproducibility; as a result, the current trend is to design a linear micronozzle that has straight walls with a specified expansion half-angle θ. The micronozzle geometry is thus a 2-D pattern that is etched into a silicon wafer or other substrate material. Depending on the microfabrication technique implemented, micronozzle depths typically range from 10–300 μm. The result is a 3-D micronozzle with a rectangular cross section [19]. A scanning electron microscopy image of the prototype MEMS-based monopropellant microthruster developed at NASA Goddard Space Flight Center (GSFC) [20] in collaboration with the University of Vermont is shown in Fig. 1 (top), in which the converging–diverging supersonic nozzle has been circled for clarification, and a schematic drawing of the nozzle is provided in Fig. 1 (bottom). As an illustration, the viscous subsonic layer is shown schematically and the thickness of the subsonic layer at the micronozzle exit is indicated. Note the 2-D nature of the sonic line at the nozzle throat.

A. Model for H_2O_2 Monopropellant

In this study, we focus our attention on the performance of monopropellant-based microthrusters. In particular, we consider decomposed high-purity (85%) hydrogen peroxide (H_2O_2) as a potential monopropellant. A monopropellant scheme is attractive for micropropulsion, due to the relatively high energy density and simplicity of implementation. Hydrogen peroxide is considered a green monopropellant and has been chosen for the development process based on its nontoxicity and relative ease of handling. Decomposition of the H_2O_2 monopropellant occurs in a catalytic chamber upstream of the nozzle inlet according to the one-step reaction:

$$2H_2O_2(l) \rightarrow 2H_2O(g) + O_2(g) + \text{heat} \tag{1}$$

where typically Silver (Ag) or Ruthenium Oxide (RuO_2) is used as a catalyst. Chemical equilibrium and thermodynamic properties of the decomposed monopropellant mixture have been calculated from

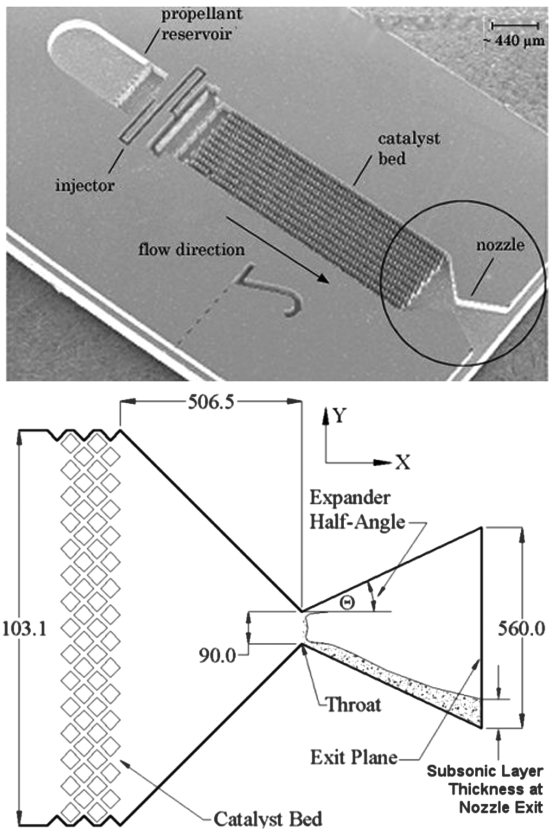

Fig. 1 Scanning electron microscopy image of the prototype microthruster (top) and geometry of the micronozzle (bottom). All dimensions are shown in microns.

NASA's Chemical Equilibrium and Application program (CEA). The CEA calculates chemical equilibrium product concentrations from a given set of reactants and determines thermodynamic and transport properties for the product mixture. The CEA database includes thermodynamic and transport properties for over 2000 species and is widely used by the aerodynamics and thermodynamics communities [21,22]. The decomposed monopropellant has been shown to be a homogeneous, frozen (nonreacting) mixture whose thermophysical properties are determined via a mass weighted average of individual component properties of the decomposed monopropellant [23].

The micronozzle inlet gas temperature is assumed to be that of the fully decomposed adiabatic flame temperature of 85%-pure decomposed H_2O_2 ($T_0 = 886$ K). The inlet stagnation pressure as a function of time ($p_0(t)$) is shown in Fig. 2 and has been chosen based on a steady-state target thrust level in range of 1–20 μN.

The adiabatic flame temperature, or stagnation temperature T_0, along with the specified stagnation pressure $p_0(t)$ establish the inlet pressure boundary condition for the micronozzle simulations. The corresponding Reynolds number for the flow (typically measured at the micronozzle throat) as a function of time is given by

$$Re(t) \equiv \frac{\dot{m}(t)L}{\mu A} \tag{2}$$

where $\dot{m}(t)$ is the time-varying mass flow rate per unit depth, L is the characteristic length scale (e.g., the 90 μm nozzle throat), μ is the dynamic viscosity of the decomposed monopropellant, and A is the cross sectional area. The value of $\dot{m}(t)$ can be well estimated from quasi-1-D theory according to [24]

$$\dot{m}(t) = \frac{p_0(t)A^*}{\sqrt{T_0}} \sqrt{\frac{\gamma}{R}\left(\frac{2}{\gamma+1}\right)^{(\gamma+1)/(\gamma-1)}} \tag{3}$$

where A^* is the nozzle throat cross section, γ is the ratio of specific heats, and R is the universal gas constant.

B. Microvalve Considerations

The focus of this study is to characterize micronozzle flow response and performance during transient operation. A typical firing of the microthruster is achieved by the opening and closing of a microvalve, which allows pressurized fuel to flow from the plenum and into the catalyst chamber before the gaseous products enter the converging–diverging supersonic micronozzle. Over the past 20 years significant progress has been made in the development of microscale valves and actuation mechanisms. However, this component of the microthruster continues to be an active area of research and development, as there are many desirable improvements to be made in the performance of existing microvalves. In fact, microvalves represent a significant hurdle in the successful miniaturization of microfluidic systems [25]. Many types of microvalves exist and they are typically described as either active or passive; here, we are concerned only with active valves, as they provide the capabilities necessary to control fuel delivery. Within the category of active microvalves, there exist several actuation mechanisms that are pertinent to microthruster applications including the following: magnetic, electric, piezoelectric, thermal, electrochemical, phase change, modular, and pneumatic, among others, all of which exhibit their own unique advantages and disadvantages. However, regardless of the design type, the defining feature of any microvalve is the actuation profile as a function of time. This is the primary characteristic of interest for design purposes. A brief summary of microvalves and their available properties is provided in Table 1.

Unfortunately, pressure and mass flow rate profiles have not been well characterized for microvalves. As such, we must make a reasonable estimate of the actuation profile for the purpose of this transient micronozzle study. A single thruster firing is simulated by adjusting the nozzle inlet stagnation pressure with duty-cycle time in order to appropriately model startup, steady state, and shutdown of the thruster. The micronozzle inlet pressure profile is thus modeled as a hyperbolic tangent for the startup and shutdown segments of the duty cycle. This represents typical solenoid valve actuation and is loosely based on the Moog microvalve prototype [26].

C. Numerical Implementation

1. *Grid Construction*

Computational domains are based upon typical nozzle geometries of the original hydrogen peroxide microthruster prototype developed at NASA GSFC; further details on this front can be found in Hitt et al. [20]. The expander half-angle θ is varied between 10 and 50° in 10° increments; all other geometric parameters are held constant, as shown in Fig. 1. Two-dimensional computational grids have been developed using Fluent Inc.'s GAMBIT 2.1 mesh generation software, and an example is provided in Fig. 3. The throat and exit dimensions of the NASA GSFC prototype (90 and 560 μm, respectively) yield an area expansion ratio of ~6.22 and is a fixed parameter in this study. To maintain the constant-area expansion ratio as the expander half-angle varies, the axial length of the expander section must be adjusted accordingly. The grids vary in size between 45,000 and 75,000 total elements, depending on the expander angle. All mesh elements are quadrilateral, with a maximum skewness of 0.5 occurring in less than 4.7% of the elements. Planar symmetry is also used in order to reduce computational expenditure. In developing the final meshes, a systematic grid refinement study has been undertaken to ensure that all results are insensitive to further grid refinement [19]. The refinement study examined grid sensitivity at both the low and high ends of the flow regime (Reynolds number) considered in this study. Accuracy of the numerical model has been verified by comparing steady-state results with the experimental work by Ketsdever et al. [14].

2. *Continuum Modeling and Boundary Conditions*

The 2-D flowfield in the micronozzle is governed by the conservation equations of mass, momentum, and energy for the fluid mixture according to

$$\frac{\partial}{\partial t}\rho + \nabla \cdot (\rho \mathbf{V}) = 0 \tag{4}$$

Table 1 Active microvalve actuation types with other relevant properties[a] [25]

Type	Material	Fluid	Actuation time, ms	Maximum pressure, kPa	Measured flow, μl/ min
EM	Fe	G	10	——	500,000
EM*	Si/Cu	L	1.5 open, 0.5 close	6900	——
ES	Si	G	0.1	——	0.87
PE	PI	N2	2	193	——
BM	Ni/Si	Air	200	1035	1,000,000
TP	PDMS	L	150	——	——
TP	PDMS	DI water	25,000	——	——
SMA	NiTi	L	660	——	——
SMA	NiTi	L	1000	207	16,800
EM + ES	Si	G	0.4	——	3000

[a]EM, electromagnetic; EM*, Moog microvalve [26]; ES, electrostatic; PE, piezoelectric; BM, bimetallic; TP, thermopneumatic; SMA, shape memory alloy; G, gas; L, liquid; and DI, deionized water.

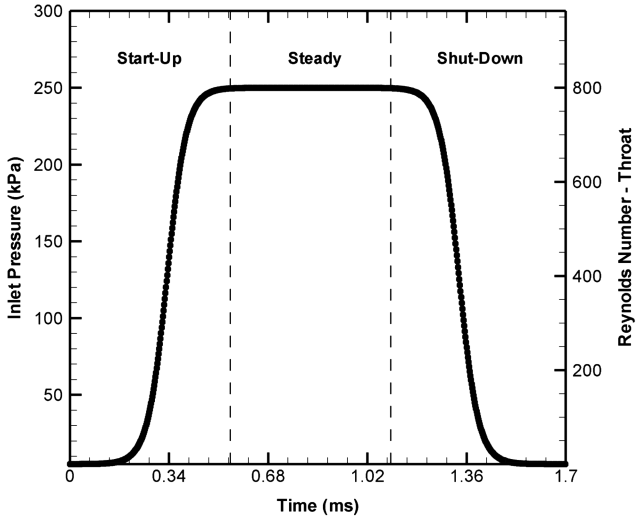

Fig. 2 Hyperbolic-tangent valve actuation profile. For reference, the throat Reynolds number corresponding to the inlet pressure is shown.

$$\frac{\partial}{\partial t}(\rho \mathbf{V}) + \nabla \cdot (\rho \mathbf{V}\mathbf{V}) = -\nabla p + \nabla \cdot (\boldsymbol{\tau}) \tag{5}$$

$$\frac{\partial}{\partial t}(\rho E) + \nabla \cdot (\mathbf{V}(\rho E + p)) = \nabla \cdot (k \nabla T + (\boldsymbol{\tau} \cdot \mathbf{V})) \tag{6}$$

$$E = h - \frac{p}{\rho} + \frac{\mathbf{V}^2}{2} \tag{7}$$

$$\boldsymbol{\tau} = \mu((\nabla \mathbf{V} + \nabla \mathbf{V}^T) - \tfrac{2}{3}\nabla \cdot \mathbf{V}\mathbf{I}) \tag{8}$$

where t is the flow time, ρ is the fluid density, $\mathbf{V}$ is the velocity vector, p is the absolute local pressure, E is the total energy, μ is the fluid viscosity, k is the thermal conductivity, T is the static temperature, h is the enthalpy, and $\boldsymbol{\tau}$ is the viscous stress tensor. The system of equations is closed by the ideal-gas-law equation of state:

$$p = \rho R T \tag{9}$$

Note here that the Nelson–Obert generalized compressibility chart has been used to verify ideal-gas behavior within the nozzle and over the range of pressures occurring throughout the duty cycle.

The thermal state of the micronozzle walls are modeled as adiabatic. This can be justified as follows. The operation of a micronozzle as a component in a micropropulsion system is inherently of limited (and often quite short) duration (typically $\ll 1$ s). In this work, the entire duty cycle is composed of 1.7 ms of flow duration. The flow response time to valve actuation is much shorter than the time scale associated with heat transfer. Thus, it is quite reasonable to regard the process as adiabatic. This notion is further supported by the results in, for example, [13,27].

A continuum flow model is assumed for this study, and thus subsonic portions of the outlet boundaries are prescribed a constant ambient backpressure value of 1.0 kPa. This value serves to maintain the Knudsen number Kn within the continuum regime with the possible exception of some slip flow regime conditions at the boundaries for the lowest Reynolds numbers considered. Continuum modeling of the micronozzle flowfield has been previously validated in [28], where a favorable comparison with DSMC simulations was observed. We mention here that the 1.0 kPa boundary pressure is imposed only at domain outlet locations where the flow is subsonic. For supersonic portions of the domain outlet, the pressure and all other flow quantities are extrapolated from the interior flow via the method of characteristics (Riemann invariants).

Initial simulations were performed under the assumption of a no-slip boundary condition. A posteriori calculations of the Knudsen number obtained from initial simulation data show values of $Kn < 0.01$ within the nozzle region for the moderate-to-high Reynolds numbers examined. This is consistent with the no-slip assumption. However, Knudsen number calculations at the lowest Reynolds numbers (early startup and late shutdown) indicate localized values of Knudsen number that are typically associated with the wall slip regime. Considering that the startup and shutdown phases combine to represent approximately two-thirds of the duty cycle, it is plausible that the effects of wall slip may have a measurable impact on performance and impulse delivered when integrated over the entire duty cycle.

To further examine the impact of potential wall slip, a new set of calculations was performed that imposed first-order slip conditions. A tangential momentum accommodation coefficient of 0.85 was imposed based on experimental data for highly polished silicon [29]. The slip condition thus corresponds to the ideal case of minimum surface roughness. In an actual device, however, the presence of surface roughness (whether the result of fabrication limitations or surface contamination) will reduce the impact of slip, and one would expect behavior approaching no-slip wall boundaries. In this regard, we have performed simulations representing the two possible scenarios for the wall momentum boundary condition. This serves to provide a comprehensive assessment of transient micronozzle performance.

3. *Computational Schemes*

The inlet boundary condition is a prescribed stagnation pressure $p_0(t)$ that resembles realistic microvalve actuation [25]. The valve actuation profile is a hyperbolic-tangent curve shown in Fig. 2. This profile is imposed on the boundary by means of a time-dependent user-defined function. A second-order implicit temporal formulation is executed with a step size $\Delta t = 10^{-5}$ s. In determining the appropriate time-step size, a systematic approach of successive reductions for Δt has shown that simulation results are insensitive to time-step size and thus resolved in time to less than 0.1% variation in total impulse delivered and impulse efficiency. Documentation of insensitivity to time-step size is provided in Table 2, which shows the impulse delivered, the percentage change in impulse, and the percentage change in impulse efficiency during the startup portion of the actuation cycle as a function of the time-step size used in the time-interval refinement study; all percentage changes are computed relative to values for the preceding time-increment size. A coupled implicit density-based solver is used with a second-order upwind discretization scheme for the convective terms.

The zeroth time step is realized by iterating to a converged steady solution that corresponds to the flowfield at time $t = 0$ s. This provides the starting point for time advancement. From this, the transient user-defined function is applied to the stagnation pressure inlet boundary according to Fig. 2. At each time step, the solution is iterated until it has converged and is then advanced in time.

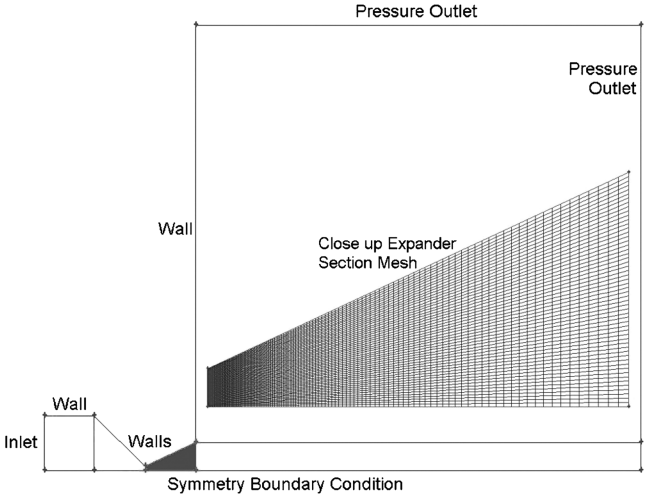

Fig. 3 Example of the computational domain and relevant boundary conditions. For clarity, the mesh in the expander region is shown as an inset.

Table 2 Tabulated results for time-increment sensitivity study for the startup portion of the actuation cycle for a 30° expander with no-slip wall conditions

Time-step size $\Delta t(s)$	Number of time steps in duty cycle	Impulse I μN · s/μm	% change in impulse I[a]	% change in efficiency η[a]
4×10^{-5}	43	5.8190×10^{-3}	——	——
2×10^{-5}	86	6.4656×10^{-3}	10	10
1.2×10^{-5}	143	6.4818×10^{-3}	0.25	0.2
1.0×10^{-5}	170	6.4870×10^{-3}	0.08	0.005
6×10^{-6}	285	6.4874×10^{-3}	0.006	0.0008

[a]All percentage changes are computed relative to values for the preceding time increment.

Convergence of the solution at a given time step is assessed via residuals and monitors for key flow quantities (e.g., $\dot{m}$) at selected locations within the domain.

Initially, the microvalve is closed and there is no pressure gradient across the nozzle and thus no flow. Once the startup sequence begins, the microvalve begins to open, the inlet pressure increases, and a pressure gradient is established across the nozzle, which begins to generate mass flow [see Eq. (3)]. The startup sequence is defined as the period from time $t = 0$ s to the time when the inlet stagnation pressure reaches 99% of the steady-state inlet pressure [p_0(steady)= 250 kPa]. Startup occurs for the initial 0.55 ms of valve actuation. The micronozzle is then operated at steady state for 0.55 ms at an inlet stagnation pressure of 250 kPa, which generates a maximum throat Reynolds number of $Re \sim 800$. The shutdown sequence begins at 99% of p_0(steady), which occurs at time $t = 1.10$ ms. The entire duty cycle occurs over 1.7 ms and includes a total of 170 time steps.

D. Thrust, Impulse, and Efficiency

In this study we are concerned with evaluating micronozzle performance including thrust production as a function of time, total impulse, and impulse efficiency. The thrust at any instant of time is formally calculated from the simulation data according to

$$\mathbf{F}(\mathbf{t}) = \int_{A_{\text{exit}}} \rho \mathbf{V}(\mathbf{V} \cdot \mathbf{n})\, \mathrm{d}A + \int_{A_{\text{exit}}} (p_{\text{exit}} - p_\infty)\, \mathrm{d}A \tag{10}$$

where p_{exit} is the pressure at the exit plane of the nozzle and p_∞ is the ambient backpressure (1.0 kPa). Throughout our simulations, the pressure thrust term is negligible in comparison with the momentum thrust.

The impulse generated for any interval of interest during the duty cycle is given by

$$\mathbf{I} = \int_{t_i}^{t_f} \mathbf{F}(\mathbf{t})\, \mathrm{d}t \tag{11}$$

where t_i and t_f are the start and end times of interest. The total impulse for the duty cycle modeled in this paper is found by taking $t_i = 0$ and $t_f = 1.7$ ms. With appropriate selection of t_i and t_f, the impulse can also be determined for isolated segments of the duty cycle: i.e., the impulse generated during startup or shutdown.

Another quantity of interest is the impulse efficiency η. This quantity is defined as the ratio of the realized impulse $\mathbf{I}$ to the maximum possible impulse $\mathbf{I}_{\max}$, defined by a quasi-1-D inviscid flow responding *instantaneously* to the valve profile. The impulse efficiency is thus given as

$$\eta = \frac{I}{I_{\max}} = \frac{\int_{t_i}^{t_f} \mathbf{F}(\mathbf{t})\, \mathrm{d}t}{\int_{t_i}^{t_f} \mathbf{F}_{\max}(\mathbf{t})\, \mathrm{d}t} \tag{12}$$

where $\mathbf{F}(\mathbf{t})$ is the thrust production given by Eq. (10), and $\mathbf{F}_{\max}(t)$ is determined from quasi-1-D inviscid theory according to

$$\mathbf{F}_{\max}(\mathbf{t}) = [(\rho_{\text{exit}} \times \mathbf{V}_{\text{exit}}^2) + (p_{\text{exit}} - p_\infty)] A_{\text{exit}} \tag{13}$$

and $\mathbf{V}_{\text{exit}}$ is calculated as

$$\mathbf{V}_{\text{exit}} = \frac{p_0 A^*}{\rho_{\text{exit}} A_{\text{exit}} \sqrt{T_0}} \sqrt{\frac{\gamma}{R}} \left(\frac{2}{\gamma + 1} \right)^{\left(\frac{\gamma+1}{\gamma-1}\right)} \tag{14}$$

with ρ_{exit} and p_{exit} determined from quasi-1-D isentropic flow relations (e.g., [24]). The calculation for $I_{\max}$ over the entire duty cycle yields a value of ~ 0.035 μN · s per micron of nozzle depth.

III. Numerical Results

In this section, we first present illustrations of the transient flowfield in the 30° expander as a point of reference for visualization of the flow behavior. Next, using simulation data we construct time-varying thrust curves for different nozzle expander half-angles ranging from 10–50° for both the slip and no-slip wall boundary conditions. The corresponding results for nozzle efficiency are then discussed. This includes the total impulse and impulse efficiency over the entire duty cycle, along with impulse efficiencies for three isolated segments of the duty cycle; mainly, the startup, steady state, and shutdown portions of valve actuation. We close with a discussion regarding the nature of the slip and no-slip wall conditions and their role in characterizing the flowfield, subsonic layers, and nozzle performance.

A. Transient Flow Response

To provide an overall illustration of the flowfield response, the sequence of the Mach contours in a 30° expander is depicted in Fig. 4 for selected time steps that include subsonic flow during startup, the transition to supersonic flow, steady-state operation, and the shutdown sequence.

During startup, the pressure ratio across the micronozzle is initially very small, the flow is overexpanded, and free boundary shock reflection occurs, as can be seen in Fig. 4 for $t \leq 0.30$ ms. As time increases during firing, the pressure ratio increases and the mass flow rate [Eq. (3)] and size of the exhaust plume increase accordingly. During this process the flowfield transitions from overexpanded $t < 0.32$ ms through perfectly expanded flow at $t = 0.32$ ms and, finally, to underexpanded exit flow, where an expansion fan develops at the nozzle exit. The steady-state portion of the duty cycle occurs during the time range of 0.55–1.10 ms and is shown in Fig. 4 represented by time $t = 0.8$ ms. During the shutdown sequence of the thruster duty cycle, the startup process and flow behavior are essentially repeated, but in reverse order. The flow response and flowfield characteristics are well explained by conventional gas dynamics and depict expected nozzle flow and plume behavior.

It should be noted that flowfield details may be less accurate far downstream of the nozzle exit plane and in the exhaust plume, due to rarefaction effects that are not accounted for with a continuum model. However, in designing a supersonic thruster nozzle, the level of accuracy required in the modeling of the plume region is really a matter of interest. For example, if the interest lies in the chemical signatures of the exhaust plume, or perhaps the interaction of the plume with a spacecraft's solid surfaces, then flow rarefaction cannot be ignored. On the other hand, if thrust production by the nozzle is the key item of interest, as is the case for this work, then the specifics of the supersonic plume are of no real import. As such, any model inaccuracies accrued within the exhaust plume *do not* affect thrust and performance calculations, as the flow remains in the continuum regime within the nozzle and up to exit (where thrust is calculated) and so the focus and approach of this study remain valid.

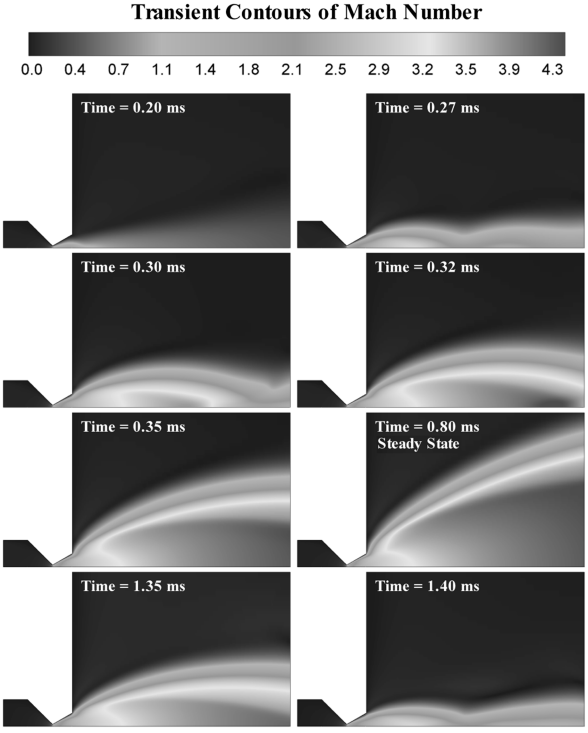

Fig. 4 Evolution of the nozzle flowfield and exhaust plumes for the 30° expander with no-slip nozzle walls.

B. Thrust Profiles

As the flow responds to the transient inlet pressure profile, the thrust output as a function of time has been calculated according to Eq. (10) and is shown in Fig. 5. Results for the slip and no-slip wall conditions are provided in units of μN/μm as well as normalized by the steady-state quasi-1-D value ($\sim$34 μN/μm). For clarity, only the 10, 30, and 50° nozzle configurations are shown at every fifth time step, and the calculations themselves are performed for every time step. All of the thrust curves display a similar trend, and the 50° expander exhibits a thrust level that is $\sim$10% less than the thrust produced by the other nozzle geometries at steady state. In general, the 30° expander demonstrates maximum thrust production.

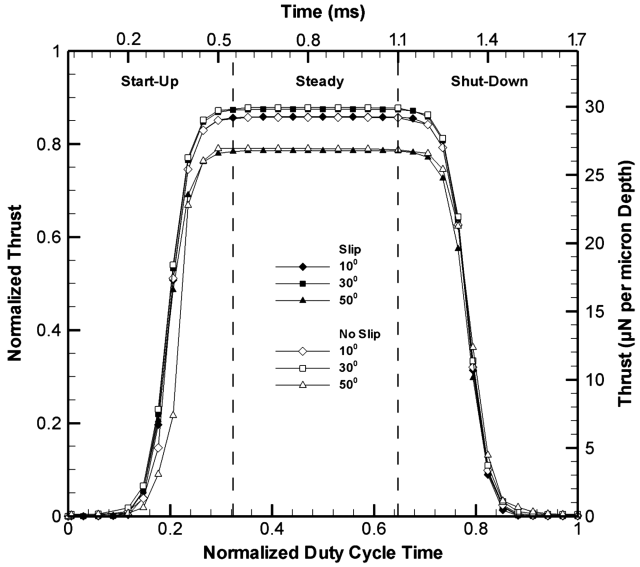

Fig. 5 Transient thrust profiles for a single thruster firing. Thrust results have been normalized by steady-state quasi-1-D theory, and the duty-cycle time has been normalized by the total valve actuation time of 1.7 ms. For clarity, data points are shown for every fifth time step.

Figure 6 presents a zoomed-in view of the thrust profiles during startup and shutdown. Here, we see that during startup all of the simulations exhibit varying amounts of thrust lag, compared with quasi-1-D flow. This lag is a direct result of viscous forces and the subsonic layer. However, during shutdown there is not a lag. All thrust curves are below the quasi-1-D inviscid prediction (i.e., ahead of the shutdown actuation profile), and thus no residual thrust production occurs. As the inlet pressure decreases during shutdown, viscous forces enhance the shutdown response by reducing flow and the corresponding thrust production.

Upon initial inspection of the complete thrust profile in Fig. 5, the results show little evidence of disparity when comparing the slip and no-slip results. However, a closer look at the thrust curves, as shown in Fig. 6, reveals a couple exceptions. First, when considering the 30° expander, it is found that the no-slip case outperforms the case with wall slip. Second, for no-slip walls there is an obvious response lag during startup in the 50° expander and a slight lag in the 10° expander relative to the slip cases. These results are a direct consequence of viscous forces and the subsonic layer. During startup, the flow must overcome viscous forces in the expander and push aside the subsonic layer in order to allow the flow to undergo supersonic expansion and generate thrust. This notion is supported by previous results in [19], where it was shown that micronozzles with 10 and 50° expander half-angles exhibit the largest subsonic layers, and micronozzles with 30° expanders have the smallest subsonic layers. During the shutdown sequence, the disparity in thrust profiles between slip and no-slip cases is less pronounced.

It is perhaps surprising that in the case of a 30° expander, the no-slip simulations outperform those with wall slip. A comparison and analysis of the influence of wall boundary conditions on micronozzle performance will be considered later in this paper.

C. Impulse and Efficiency

Attitude control of the spacecraft is achieved by applying discrete impulse bits and so the total impulse delivered during a single firing is a key parameter of interest. Similarly, the operational impulse efficiency of a given nozzle design is another measure of interest. Total impulse delivered, in (μN · s)/μm, and the impulse efficiency η for a single duty cycle have been calculated according to Eqs. (11) and (12), respectively, and are presented in Fig. 7 for both the slip and no-slip boundary conditions. It is seen that the impulse and efficiency exhibit a maximum for expander half-angles in the range of 25–30°. For $\theta > 30°$ there is a sharp decrease in efficiency and total impulse delivered: a direct consequence of geometric losses associated with large expander angles. There is a less obvious decline in total impulse and efficiency for $\theta < 30°$. Performance degradations at small expander angles (or, equivalently, lengthened expanders) are a consequence of increased viscous losses associated with the correspondingly increased subsonic layer.

When comparing the slip versus no-slip results of Fig. 7, it is found that as the half-angle is reduced to $\theta < 30°$, the impulse efficiency for the slip condition does not depreciate as fast as the no-slip condition. This can be attributed to the reduced influence of viscous forces at the slip wall boundary. As such, the slip simulation data shown in Fig. 7 are characterized by a performance plateau over the range of $15° < \theta < 30°$, and the no-slip data display a more pronounced peak corresponding to $\theta = 30°$. For $\theta > 30°$, both sets of data exhibit similar results, as performance is governed by geometric losses and the wall boundary condition plays a much weaker role.

The characterization of impulse efficiency affords an opportunity to isolate and compare the three segments of the duty cycle. This is accomplished by selecting appropriate t_i and t_f in Eq. (12) in order to isolate the impulse produced during startup, steady state, and shutdown, as demarcated on the actuation profile in Fig. 2. We have computed the impulse efficiency for the three segments of the duty cycle and the data appear in Fig. 8. It is clear that the steady-state portion of the duty cycle demonstrates the highest impulse efficiency, with a maximum of $\sim$87% corresponding to the 30° expander and an average of $\sim$85% over the range of expander angles studied.

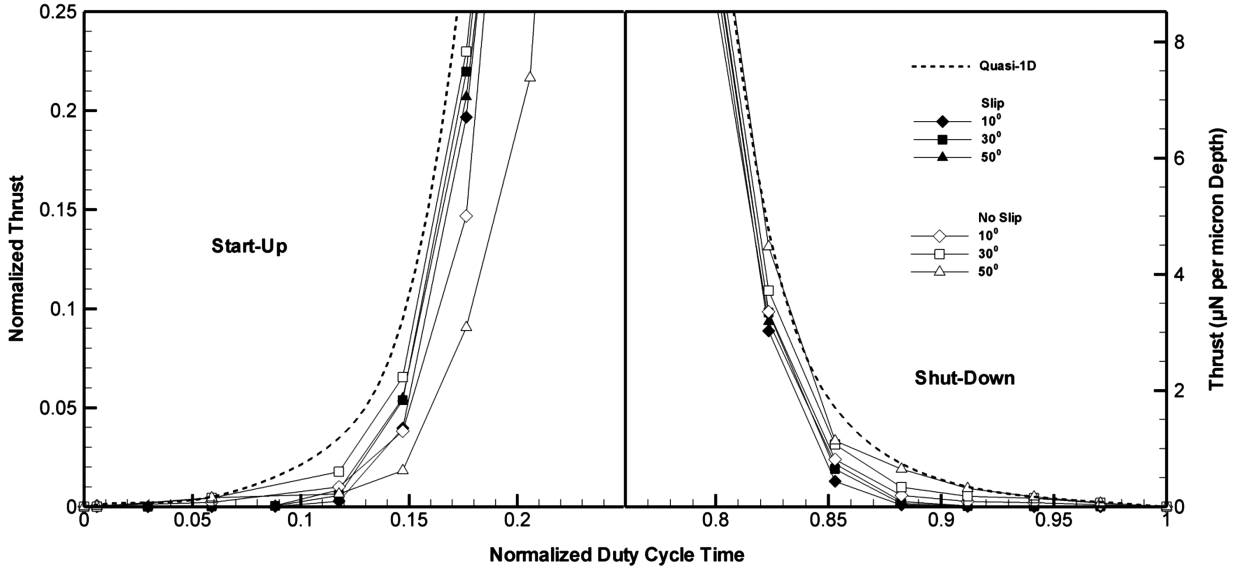

Fig. 6 Zoomed-in view of thrust response during flow startup (left) and shutdown (right). For clarity, data points are shown for every fifth time step.

The startup sequence shows the lowest impulse efficiency, with an average of ∼81% over the range of expander angles examined and a minimum of ∼76% corresponding to the 50° expander. This is a consequence of the fact that the subsonic layer initially occupies the entire expander and the flow must overcome viscous forces and the established subsonic layer. The shutdown sequence shows only a slightly improved efficiency over startup (∼1%) as viscous forces actually facilitate the flow response by reducing flow during valve closure.

We next compare the efficiencies of the three duty-cycle segments for the slip and no-slip boundary conditions. It is apparent in Fig. 8 that the steady-state portion of the cycle shows a negligible difference between the slip and no-slip results. At the relatively large Reynolds numbers associated with steady state, geometry is the governing parameter; thus, the wall boundary condition type is not influential and there is minimal disparity between the slip and no-slip results. At the reduced Reynolds numbers found during startup and shutdown, viscous forces are the governing parameter. Previous analysis that have shown that the subsonic layer is largest in micronozzles with expanders of $\theta < 20$ and $>40°$ [19], and thus the slip boundary condition yields a higher efficiency at the high and low ends of the expansion angles considered. This result can be attributed to the fact that the slip boundary condition reduces flow resistance at the wall. For the slip simulation results, we again see a performance plateau for expander half-angles ranging from 15–30° for all three segments of the duty cycle. However, in cases where viscous forces are balanced by geometric compensations (i.e., expansion half-angles in the range of $25° < \theta < 35°$ [19]), the no-slip simulations realize a higher efficiency (see Figs. 5–8, $\theta = 30°$). For the no-slip simulations, we see a more pronounced peak in the efficiency curves corresponding to $\theta = 30°$. An analysis and discussion of the simulation data, which show no-slip micronozzles outperforming those with wall slip, are the foci of the following section.

D. Role of Wall Boundary Conditions

In the preceding results, differences in flowfield characteristics and performance have been observed between micronozzles with slip and no-slip walls. In this section, we examine the physical nature of the boundary condition in greater detail to provide insight into the role of the boundary condition. Furthermore, we seek to delineate the effects on subsonic boundary-layer evolution and the impact on nozzle thrust, impulse, and performance response during the transient firing of the thruster.

First we focus our attention upon the startup sequence of the duty cycle in order to examine the influence of the wall boundary condition on the evolution of subsonic-layer growth. Figure 9 compares the size of the subsonic layer in a 30° expander for both slip

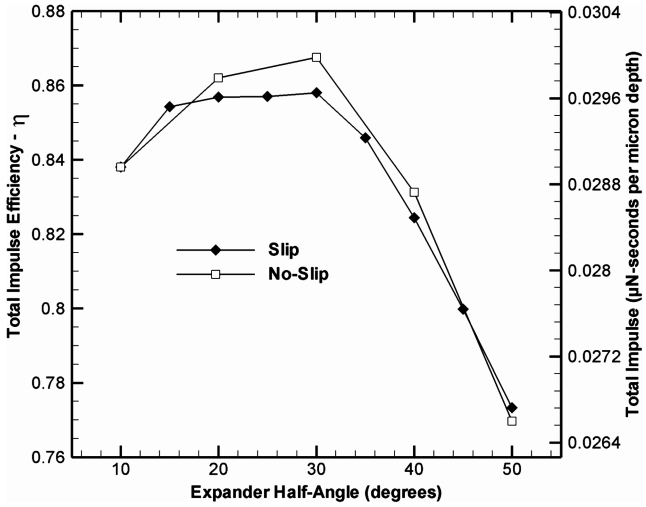

Fig. 7 Total impulse generated by the micronozzle during a single duty cycle.

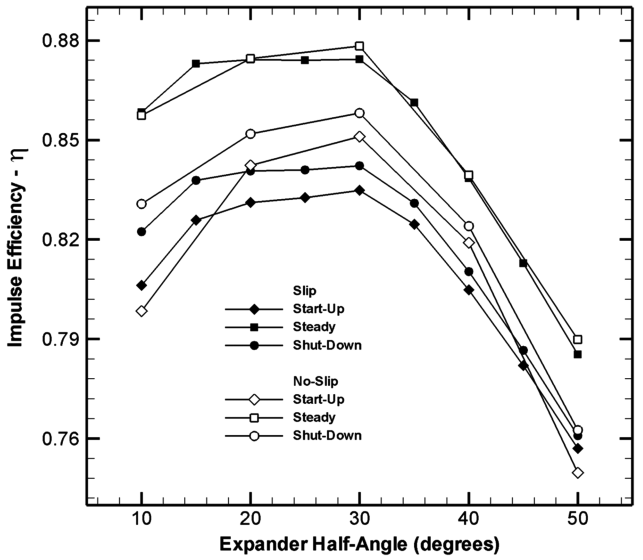

Fig. 8 Impulse efficiency shown for the three segments of the duty cycle.

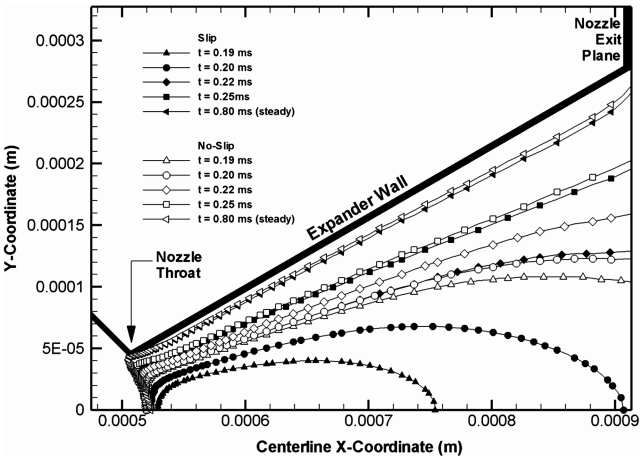

Fig. 9 Comparison of slip and no-slip subsonic-layer evolutions in the 30° expander during flow startup. Note that the subsonic layer is larger for the slip condition.

and no-slip conditions at four selected time steps during startup as well as at steady state. The curves shown are isolines for $M = 1$ and the subsonic region lies between the curve and the expander wall. The supersonic portion of the flow is between the curve and the nozzle centerline. For any time step, there is a larger subsonic region for the slip flows and, although not explicitly shown, similar observations are found during shutdown. During startup, the transition from subsonic to supersonic flow is slower for slip flows than for the equivalent no-slip case. Evidence for this is shown in Fig. 9 in that the difference in subsonic layer between slip and no-slip decreases with time and a minimal difference exists at steady state. The consequence of an increased subsonic layer for slip flows is reflected in the Mach profile at the nozzle exit plane. In Fig. 10 it is observed that at any time step the Mach number profile for nozzles with wall slip is less than the Mach number for the no-slip case across the entire exit plane cross section.

Further analysis of the flowfield shows that these results are explained by continuity considerations as follows. The slip boundary condition, by definition, allows for a net momentum in the flow direction to exist at the wall itself. As such, the local mass flow in the near-wall region is greater for nozzles with wall slip. If we define the near-wall region of interest as the portion of the flowfield contained within the subsonic layer, then we are able to quantify and compare the disparity in mass flow through the subsonic layer for the slip and

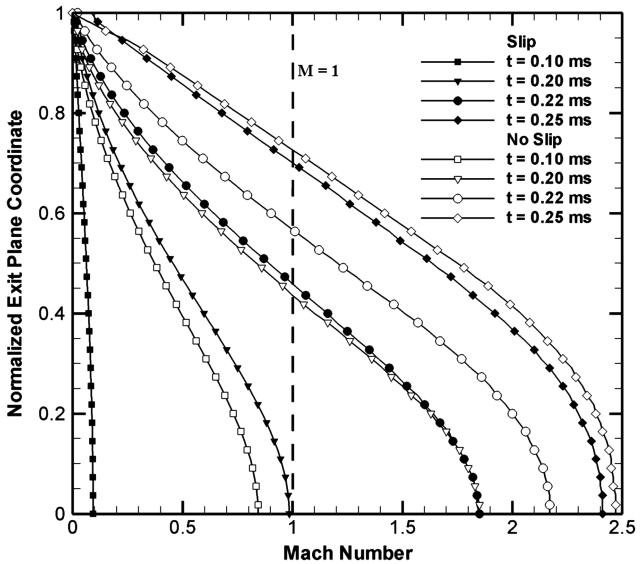

Fig. 10 Mach number profile at the nozzle exit plane at selected times during startup. Note that the Mach number is larger for the no-slip condition.

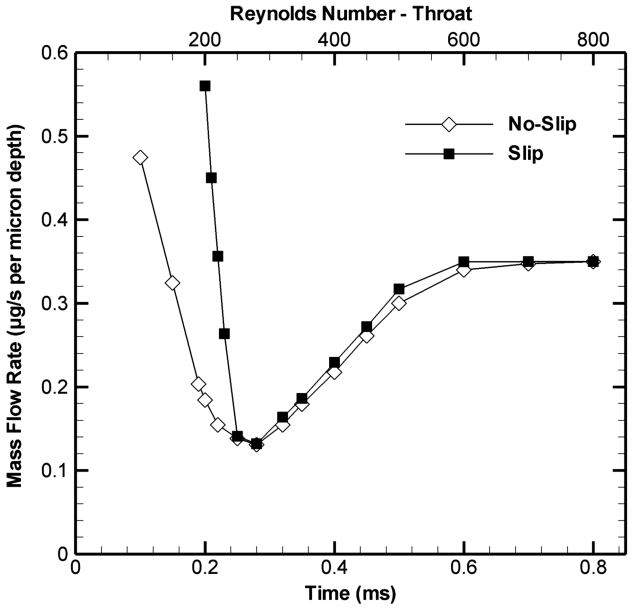

Fig. 11 Comparison of mass flow rates in the subsonic layer for slip and no-slip walls in a micronozzle with a 30° expander half-angle.

no-slip flows. We have calculated the mass flow rate contained within the subsonic layer at the micronozzle exit plane, and these results are presented in Fig. 11 for startup times where the subsonic layer occupies less than 100% of the exit plane and up to the steady-state condition. (Time steps associated with a totally subsonic exit are not considered here.) In Fig. 11 it is found that the slip condition does indeed allow more mass to flow through the subsonic layer, compared with the no-slip case. This disparity is particularly pronounced at small times, diminishes with time, and eventually approaches zero at steady state ($t = 0.8$ ms, $Re \sim 800$). The negligible difference at steady state is due to the relatively large Reynolds number at that stage.

It is interesting to note that as the startup sequence progresses, the evolution of the mass flow rate through the subsonic layer (whether a slip or no-slip boundary condition) is not monotonic. There is an initial decrease due to the fact that the size of the subsonic layer itself decreases (Fig. 9). However, the profile of the subsonic layer asymptotes to its steady-state configuration before the inlet pressure reaching its maximum value. The mass flow through the subsonic layer, and the micronozzle as a whole, will subsequently increase as the inlet pressure continues to increase to its steady-state value. This can be seen in Fig. 11 for the time steps greater than 0.28 ms. Note that no-slip walls allow less mass to flow through the subsonic layer. To satisfy continuity in the no-slip case, mass is forced into the supersonic core, and thus a larger percentage of the mass flow is supersonic. This results in improved performance compared with identical micronozzle flows with slip walls.

At the very low Reynolds numbers occurring early during startup, the no-slip condition actually increases thrust production, as continuity forces a larger percentage of the mass flow into the supersonic core, where gas behavior more closely resembles a quasi-1-D flow. The slip condition, on the other hand, allows more mass to pass through the subsonic layer, *but at a reduced speed*, compared with the supersonic core of the flow. It is this allocation of mass flow across the expander cross section in order to maintain continuity that allows micronozzles with no-slip walls to outperform those with slip walls (see Fig. 8).

IV. Conclusions

Supersonic micronozzle flow represents a unique flow regime characterized by supersonic Mach numbers and very low Reynolds numbers. In this study, our goal has been to characterize transient micronozzle flow and performance via the simulation of a realistic microvalve duty cycle using a H_2O_2 monopropellant scheme. For

MEMS-based micronozzles with varying expander angles, the thrust production as a function of time has been delineated, along with the total impulse delivered during a single firing and nozzle impulse efficiencies have been determined based on theoretical maximum performance. Finally, the role of nozzle wall boundary conditions has been examined. This includes the highly polished slip condition and the severe roughness of a surface exhibiting the no-slip condition. The specific contributions of this work include detailed examinations of the following: 1) a transient supersonic micronozzle flow analysis based on a realistic valve duty cycle, 2) a variable nozzle geometry (expander half-angles 10–50°), 3) the simulation of decomposed H_2O_2 monopropellant, and 4) an analysis of the slip and no-slip wall boundary conditions.

The numerical results indicate that a lag in flow response and thrust production exists during startup for all cases examined. This lag is especially pronounced for the 10 and 50° expanders with a no-slip wall boundary condition: a result of large viscous forces and subsonic layers associated with those expander geometries and flow regime. This response delay is not observed during shutdown, as viscous forces act to reduce flow and facilitate the shutdown response.

It is found that the maximum impulse delivered and maximum impulse efficiency is achieved with an expander half-angle of 30° for the no-slip condition. The simulations of wall slip do not indicate a clear maximum corresponding to a single geometry, but rather it is found that a plateau exists in the range of $\theta = 20$–$30°$. It is worthy of note that these values are 1.5–2 times the typical half-angles used in macroscale conical thrusters [30]. The simulation data exhibit maximum efficiency during the steady-state segment of the duty cycle and the lowest efficiency occurs during startup, as a consequence of the response lag. The simulation results expose minor disparities between the slip and no-slip impulse efficiencies that vary by, at most, 1.4%, with nearly identical results during the steady-state portion of the duty cycle.

Acknowledgment

This work was supported by the U.S. Air Force Office of Scientific Research under grant no. FA9550-06-1-0364.

References

[1] Blandino, J., and Cassady, R., "Propulsion Requirements and Options for the New Millennium Interferometer (DS-3) Mission," 34th AIAA/ASME/SAE/ASEE Joint Propulsion Conference & Exhibit, Cleveland, OH, AIAA Paper 98-3331, 1998.

[2] Pollard, P., Chao, C., and Janson, S., "Populating and Maintaining Cluster Constellations in Low-Earth Orbit," 35th AIAA/ASME/SAE/ASEE Joint Propulsion Conference & Exhibit, Los Angeles, AIAA Paper 99-2871, June 1999.

[3] Helvajian, H., and Janson, S. W., *Small Satellites: Past, Present, and Future*, Aerospace Press, El Segundo, CA, 2008.

[4] Mueller, J., "Thruster Options for Microspacecraft: A Review and Evaluation of the State-of-the-Art and Emerging Technologies in Micropropulsion for Small Spacecraft," *Progress in Astronautics and Aeronautics*, Vol. 187, AIAA, Reston, VA, 2000, pp. 45–137.

[5] Reichbach, J. G., Sedwick, R. J., and Martinez-Sanchez, M., "Micropropulsion System Selection for Precision Formation Flying Satellites," 37th AIAA/ASME/SAE/ASEE Joint Propulsion Conference & Exhibit, Salt Lake City, UT, AIAA Paper 2001-3646, 2001.

[6] Bayt, R. L., and Breuer, K. S., "Viscous Effects in Supersonic MEMS-Based Micronozzles," *Proceedings of the 3rd ASME Microfluids Symposium*, Anaheim, CA, 1998.

[7] Bayt, R. L., and Breuer, K. S., "System Design and Performance of Hot and Cold Supersonic Microjets," AIAA Paper 2001-0721, 2001.

[8] Alexeenko, A. A., Levin, D. A., Gimelshein, S. F., and Collins, R. J., "Numerical Modeling of Axisymmetric and Three-Dimensional Flows in MEMS Nozzles," 36th AIAA/ASME/SAE/ASEE Joint Propulsion Conference Exhibit, Huntsville, AL, AIAA Paper 2000-3668, 2000.

[9] Alexeenko, A. A., Levin, D. A., Gimelshein, S. F., Collins, R. J., and Reed, B. D., "Numerical Modeling of Axisymmetric and Three-Dimensional Flows in Microelectromechanical Systems Nozzles," *AIAA Journal* Vol. 40, No. 5, 2002, pp. 897–904. doi:10.2514/2.1726

[10] Alexeenko, A. A., and Levin, D. A., "Numerical Simulation of High-Temperature Gas Flows in a Millimeter-Scale Thruster," *Journal of Thermophysics and Heat Transfer*, Vol. 16, No. 1, 2002, pp. 10–16. doi:10.2514/2.6667

[11] Alexeenko, A. A., Gimelshein, S. F., Levin, D. A., Ketsdever, A. D., and Ivanov, M. S., "Measurements and Simulation of Orifice Flow for Micropropulsion Testing," *Journal of Propulsion and Power*, Vol. 19, No. 4, July 2003, pp. 588–594. doi:10.2514/2.6170

[12] Alexeenko, A. A., Levin, D. A., Fedosov, D. A., Gimelshein, S. F., and Collins, R. J., "Performance Analysis of Microthrusters Based on Coupled Thermal-Fluid Modeling and Simulation," *Journal of Propulsion and Power*, Vol. 21, No. 1, 2005, pp. 95–101. doi:10.2514/1.5354

[13] Alexeenko, A. A., Fedosov, D. A., Gimelshein, S. F., Levin, D. A., and Collins, R. J., "Transient Heat Transfer and Gas Flow in a MEMS-Based Thruster," *Journal of Microelectromechanical Systems*, Vol. 15, No. 1, 2006, pp. 181–194. doi:10.1109/JMEMS.2005.859203

[14] Ketsdever, A. D., Clabough, M. T., Gimelshein, S. F., and Alexeenko, A. A., "Experimental and Numerical Determination of Micropropulsion Device Efficiencies at Low Reynolds Numbers," *AIAA Journal*, Vol. 43, No. 3, March 2005, pp. 633–641. doi:10.2514/1.10284

[15] Choudhuri, A. R., Baird, B., Gollahalli, S. R., and Schneider, S. J., "Effects of Geometry and Ambient Pressure on Micronozzle Flow," 37th AIAA/ASME/SAE/ASEE Joint Propulsion Conference and Exhibit, Salt Lake City, UT, AIAA Paper 2001-3331, 2001.

[16] Louisos, W. F., and Hitt, D. L., "Viscous Effects in Supersonic Micro-Nozzle Flows: Transient Analysis," 36th AIAA Fluid Dynamics Conference, San Francisco, AIAA Paper 2006-2874, June 2006.

[17] Kujawa, J., and Hitt, D. L., "Transient Shutdown Simulations of Realistic MEMS Supersonic Nozzles," AIAA Paper 2004-3762, 2004.

[18] Morinigo, J. A., and Quesada, J. H., "Analysis of Viscous Heating in a Micro-Rocket Flow and Performance," *Journal of Thermal Science*, Vol. 17, No. 2, 2008, pp. 116–124. doi:10.1007/s11630-008-0116-8

[19] Louisos, W. F., and Hitt, D. L., "Viscous Effects on Performance of Two-Dimensional Supersonic Linear Micronozzles," *Journal of Spacecraft and Rockets*, Vol. 45, No. 4, 2008, pp. 706–715. doi:10.2514/1.33434

[20] Hitt, D. L., Zakrzwski, C., and Thomas, M., "MEMS-Based Satellite Micropropulsion Via Catalyzed Hydrogen Peroxide Decomposition," *Smart Materials & Structures*, Vol. 10, 2001, pp. 1163–1175. doi:10.1088/0964-1726/10/6/305

[21] McBride, B., and Sanford, G., "NASA-Glenn Chemical Equilibrium Program CEA2," NASA RP-1311, Pt. 1, 1994.

[22] McBride, B., and Sanford, G., "NASA-Glenn Chemical Equilibrium Program CEA2," NASA RP-1311, Pt. 2, 1996.

[23] Vargaftik, N. B., *Thermophysical Properties of Gases and Liquids*, 2nd ed., Hemisphere, New York, 1975.

[24] Anderson, J. D., Jr., *Modern Compressible Flow with Historical Perspective*, 3rd ed., McGraw–Hill, Boston, 2003, pp. 191–235.

[25] Kwang, W. O., and Chong, H. A., "A Review of Microvalves," *Journal of Micromechanics and Microengineering*, Vol. 16, No. 5, May 2006, pp. 13–39. doi:10.1088/0960-1317/16/5/R01

[26] Mueller, J., Marrese, C., Polk, J., Yang, E., Green, A., White, V., Bame, D., Chakraborty, I., Vargo, S., and Reinicke, R., "An Overview of MEMS-Based Micropropulsion Developments at JPL," *Acta Astronautica*, Vol. 52, Nos. 9–12, May–June 2003, pp. 881–895. doi:10.1016/S0094-5765(03)00069-9.

[27] Louisos, W. F., and Hitt, D. L., "The Role of Heat Transfer on Performance of 3D Supersonic Micronozzles," 39th AIAA Fluid Dynamics Conference, San Antonio, TX, AIAA Paper 2009-3823, June 2009.

[28] Louisos, W. F., Alexeenko, A. A., Hitt, D. L., and Zilic, A., "Design Considerations for Supersonic Micronozzles," *International Journal of Manufacturing Research*, Vol. 3, No. 1, 2008, pp. 80–113. doi:10.1504/IJMR.2008.016453

[29] Arkilic, E., Breuer, K., and Schmidt, M., "Mass Flow and Tangential Momentum Accommodation in Silicon Micromachined Channels," *Journal of Fluid Mechanics*, Vol. 437, No. 29, 2001, pp. 29–44.

[30] Humble, R. W., Henry, G. N., and Larson, W. J., *Space Propulsion Analysis and Design*, McGraw–Hill, New York, 1995.

R. Cummings
Associate Editor